José del Águila Ferrandis[1]
MIT Sea Grant Design Lab,
Department of Mechanical Engineering,
Massachusetts Institute of Technology,
12 Emily St,
Cambridge, MA 02139
e-mail: jaguila@mit.edu

Luca Bonfiglio
MIT Sea Grant Design Lab,
Department of Mechanical Engineering,
Massachusetts Institute of Technology,
12 Emily St,
Cambridge, MA 02139
e-mail: bonfi@mit.edu

Ricardo Zamora Rodríguez
Canal de Ensayos Hidrodinámicos,
Escuela Técnica Superior de Ingenieros Navales,
Universidad Politécnica de Madrid,
Avda. de la Memoria no 4 - 28040,
Madrid, Spain
e-mail: ricardo.zamora@upm.es

Chryssostomos Chryssostomidis
MIT Sea Grant Design Lab,
Department of Mechanical Engineering,
Massachusetts Institute of Technology,
12 Emily St,
Cambridge, MA 02139
e-mail: chrys@mit.edu

Odd Magnus Faltinsen
Centre for Autonomous Marine Operations &
Systems (AMOS),
Norwegian University of Science and Technology,
Trondheim, Norway
e-mail: odd.faltinsen@ntnu.no

Michael Triantafyllou
MIT Sea Grant,
Department of Mechanical Engineering,
Massachusetts Institute of Technology,
12 Emily St,
Cambridge, MA 02139
e-mail: mistetri@mit.edu

Influence of Viscosity and Non-Linearities in Predicting Motions of a Wind Energy Offshore Platform in Regular Waves

Motion predictions of floating bodies in extreme waves represent a challenging problem in naval hydrodynamics. The solution of the seakeeping problem involves the study of complex non-linear wave-body interactions that require large computational costs. For this reason, over the years, many seakeeping models have been formulated in order to predict ship motions using simplified flow theories, usually based on potential flow theories. Neglecting viscous effects in the wave-induced forces might largely underestimate the energy dissipated by the system. This problem is particularly relevant for unconventional floating bodies at resonance. In these operating conditions, the linear assumption is no longer valid, and conventional boundary element methods, based on potential flow, might predict unrealistic large responses if not corrected with empirical viscous damping coefficients. The application considered in this study is an offshore platform to be operated in a wind farm requiring operability even in extreme meteorological conditions. In this paper, we compare heave and pitch response amplitude operators predicted for an offshore platform using three different seakeeping models of increasing complexity, namely, a frequency-domain boundary element method (BEM), a partly nonlinear time domain BEM, and a non-linear viscous model based on the solution of the unsteady Reynolds-averaged Navier–Stokes (URANS) equations. Results are critically compared in terms of accuracy, applicability, and computational costs. [DOI: 10.1115/1.4047128]

Keywords: computational fluid dynamics, design of offshore structures, floating and moored production systems, fluid-structure interaction, hydrodynamics, ocean energy technology

1 Introduction

Over the last 25 years, there has been an ongoing effort within the U.N. Framework Convention on Climate Change to mitigate climate change and greenhouse emissions. The latest example of these efforts is the *Paris Climate Agreement*, which was adopted in November of 2015 by consensus at the *21st Conference of Parties of the United Nations Framework Convention on Climate Change* (UNFCCC). As of May 2019, 194 states and the European Union have ratified the agreement. These states represent more than 88% of the global greenhouse gas emissions. The increasing efforts to meet the objectives of international agreements have led to significant developments of technologies to extract energy from clean renewable sources, making them economically viable. Wind energy represents one of the most promising renewable energy resources, and it is demonstrated by the increasing design and construction of onshore and shallow water wind farms, as shown by the Global Wind Energy Council[2] and the European Wind Energy Association.[3] This has enabled some countries to produce more than 35% of their electric demand from wind,[4] which proves the opportunities given by existing onshore and shallow water installations to reduce the amount of energy dependence on fossil fuels.

Space allocation represents one of the major limitations in the development of new onshore and shallow water installations. Regardless of higher installation costs, offshore wind energy

---

[1]Corresponding author.

[2]http://www.gwec.net
[3]http://www.windeurope.org
[4]See Note 3.

extraction is generally more efficient than it is for onshore installations. Higher and more sustained wind speeds have led to reduced operating condition uncertainty and have made offshore wind farms a very attractive wind energy harvesting alternative. In addition to higher construction and installation costs, the intricacy in designing a complex interacting system composed of floating structures and wind turbines operating in a marine environment has limited the spread of this promising renewable energy.

Among other problems, the prediction of the seakeeping behavior of offshore structures in adverse marine environment represents one of the greatest challenges in the design of offshore wind farms. Motion predictions of floating platforms in waves have been traditionally obtained by using potential flow based numerical models. Most of these models are formulated on the basis of a small amplitude assumption, which limits their range of applicability in cases of practical interest. Nevertheless, conventional linear seakeeping methods formulated in frequency domain still represent the most widely used seakeeping models. Furthermore, consistent second-order potential-flow solvers without accounting for current and forward speed represent state of the art numerical methods for wave-induced response of ships and other large-volume marine structures. Important viscous damping effects such as for rolling of ships and slow-drift motions of moored structures are accounted for by empirical formulas. Strongly nonlinear wave effects on ships are traditionally highly simplified by only considering Froude–Krylov and hydrostatic restoring terms. When slamming occurs, it is typically analyzed, for ships, by strip theory with a high-frequency free surface condition based on either a von Karman or a generalized Wagner method. The latter simplifications are necessitated due to computational efficiency. The stochastic response in representative sea states each with a duration of 3–5 h has to be considered.

Viscous models such as unsteady Reynolds-averaged Navier–Stokes (URANS) have been mostly applied to the solution of problems that have a large economical impact (see Refs. [1–4]) or to unconventional geometries where conventional potential flow theories fail (see Refs. [5–8]). A drawback is that URANS depends on empirical modeling of turbulence. Motion predictions obtained using viscous models are limited by the massive computational costs required to even characterize response amplitude operators (RAOs) of complex geometries in six degrees-of-freedom (6DOFs) in regular waves. One of the major bottlenecks in the application of Navier–Stokes models is that they can hardly be used for shape optimization in the earliest design stages, when there is still large uncertainty associated with the final shape of the floating body. Reducing this uncertainty would involve a large number of simulations to cover the design space, which would be extremely costly and would only be possible because averaging viscosity effects provides a good approximation in this design problem. However, given the technological improvements and cost reduction of mainstream wind energy, the potential economic impact of deepwater offshore wind energy is high enough to justify the employment of these computationally expensive high-fidelity codes. To this end, research has been recently focusing on developing computational models to enable URANS simulations for motion prediction of offshore platforms, considering non-linear effects in viscous flows. The use of higher fidelity simulations in shape optimization studies will eventually lead to improved designs capable of reducing motions in waves, hence having extended operability.

In this paper, we first present a summarized overview of the challenges related to solving the seakeeping problem and how the capabilities of each type of computational model compare to each other (Sec. 2). In Sec. 3, we provide a brief theoretical definition of the flow problem, summarizing for the applied potential flow-based boundary element method (BEM) codes and the used URANS code. Given this information and the definition of the hydrodynamic coefficients in the BEMs, it is possible to solve the motion problem. The results obtained are presented in Sec. 4, where we provide heave and pitch RAOs predicted using the frequency-domain and time-domain potential panel methods, and the high-fidelity viscous model based on the solution of the unsteady Reynolds averaged Navier–Stokes equations. The main findings are summarized in Sec. 5, where we also give an insight of what may enable a wide application of URANS simulations to motion prediction problems.

2 Challenges in Solving the Seakeeping Problem

The response of a floating body in a marine environment largely depends on the external forces and moments induced by incoming waves and on the characteristics of the system such as geometry, inertia, and mass distribution.

Fluid dynamic forces can be divided into three different categories according to their nature: inertia, gravity, and viscous phenomena. Model scale experiments can be performed in Froude similarity, which ensures an accurate representation of gravity related phenomena [9]. Due to the practical limitations of having a fluid contemporary allowing Froude and Reynolds similarity, viscous forces predicted in model experiments might be affected by scale effects, in particular if flow separation does not occur from sharp corners. Numerical simulations performed with viscous solvers, allow to predict platform motions in full scale considering the effect of viscous dissipations.

Boundary element methods are based on potential flow in a incompressible liquid; hence, they do not solve for viscous dissipations. Among BEMs, the ones formulated in the frequency domain usually do not consider non-linear effects such as the variation of the wet surface of the offshore platform. However, second-order non-linear frequency domain potential flow methods without current and forward speed are state of the art. To this end, time-domain BEMs have been introduced with the specific goal to improve predictions in cases of large amplitude motions. Successful examples of time-domain motion predictions obtained with BEMs that consider some non-linear effects can be found in the literature (see for instance Refs. [10–13]). Due to the potential flow assumption, BEMs represent a valuable method to predict motions in waves with a reasonable trade-off between computational costs and prediction fidelity [14–16]. Limitations in BEMs due to their simplified potential flow formulation are not important away from situations where non-linear phenomena becomes relevant (e.g., resonance). Therefore, URANS simulations should only be used when viscous forces are important since they are at least two orders of magnitude more computationally expensive than the potential codes.

Viscous dissipations, in the particular platform geometry considered, are important for the calculation of cancellation effects in heave and large amplitude resonant heave and pitch motions.

Cancellation effects occur in semi-submersible platforms when the resultant forces acting on the underwater pontoons and vertical pillars tend to cancel each other under linear undamped motions. Usually, the highest cancellation period is the result of the forces on the pontoons and the pillars compensating each other. Other cancellation periods result from the particular spacing of the vertical pillars. For the brazeless geometry analyzed in this study, Eq. (6) gives an accurate prediction of this cancellation period (Fig. 1).

A detailed and instructive explanation of cancellation effects can be found in Ref. [17]. This analysis is performed for a semisubmersible in beam seas and deep water waves in the frequency domain. We will generalize the approach so that it is applicable to our studied platform. An assumption is that the wavelength is
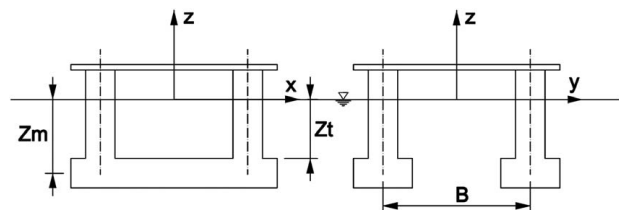

Fig. 1 Sketch of a semisubmersible platform used in Ref. [17] to show how cancellation effects in heave motions occur

sufficiently large for phase differences in the vertical hydrodynamic loads on different structural parts have negligible influence. A consequence is that the wave heading does not matter. The starting point is the undamped heave (η_3) equation of motion in the mass-force domain:

$$(M + A_{33})\frac{d^2\eta_3}{dt^2} + \rho g A_w \eta_3 = F_3(t) \qquad (1)$$

Here M, A_{33}, and A_w are the structural mass, heave added mass, and water plane, respectively. Furthermore, ρ and g are mass density of water and acceleration of gravity, respectively. The vertical excitation forces, $F_3(t)$, by potential flow can be simplified as

$$F_3(t) = \rho g \zeta_a \sin \omega t e^{k z_m}\left(A_w e^{k(z_t - z_m)} - k\left(V_p + \frac{A_{33}}{\rho}\right)\right) \qquad (2)$$

where z_t and z_m are the z-coordinates of the top and geometric center of the pontoons, respectively, and V_p is the displaced volume of the pontoons. The free surface elevation at the center plane is expressed as $\zeta_a \sin \omega t$. Since $k(z_t - z_m)$ is small, we approximate $e^{k(z_t - z_m)}$ as $1 + k(z_t + z_m)$. Furthermore, by using $M = \rho(V_p - A_w z_t)$, it follows that

$$F_3(t) = \zeta_a \sin \omega t e^{k z_m}\left(\rho g A_w - \omega^2(M + A_{33}) - \rho\omega^2 A_w z_m\right) \qquad (3)$$

Introducing the result from Eq. (3) in Eq. (1), we can express the relation between the amplitudes of the vertical motion and the free surface elevation as

$$\frac{\eta_3}{\zeta_a} = \sin \omega t e^{k\varepsilon_m}\left(1 - \frac{k z_m}{1 - \left(\frac{\omega}{\omega_n}\right)^2}\right) \qquad (4)$$

where ω_n is the natural circular frequency.

$$\omega_n = \left(\frac{\rho g A_w}{M + A_{33}}\right)^{1/2} \qquad (5)$$

By exploring Eq. (4), we can obtain the situations where the vertical heave motion is zero ($\eta_3 = 0$). This happens when

$$\omega = \frac{\omega_n}{\left(1 - |z_m|\frac{\omega_n^2}{g}\right)^{1/2}} \qquad (6)$$

In the particular geometry analyzed in this paper, this period would correspond to $T_w = 16.73$ s, which is accurately predicted with Eq. (6). Furthermore, if we would like to change the heave response characteristics, we can see from Eq. (4) that the parameters to vary would be ω/ω_n and $\omega_n^2 |z_m|/g$.

The previous analysis shows how cancellation effects arise when the vertical motion of semi-submersible platforms are studied considering linear undamped motions. This assumptions will not hold when viscous drag forces, which influence excitation and damping in a nonlinear manner, have a non-negligible effect. In the particular geometry analyzed in this paper, the nature of this damping and viscous drag forces is non-linear as the magnitude of the shed vortexes can be expected to vary throughout the motion and also with the amplitude of the motion. In this case, we will have to resort to viscous models such as URANS. Nevertheless, modeling and numerical uncertainty might affect the accuracy of the prediction of this higher fidelity models.

3 Numerical Methods

In this paper, we employ three different seakeeping models providing an increasing level of accuracy and a good representation of the methods available to designers.

3.1 Linear Frequency-Domain Boundary Element Method.
The first code used to obtain the motions of the offshore platform is ANSYS AQWA a linear BEM formulated in the frequency domain. Potential flow of incompressible water is assumed.

A basis of a BEM is Green's theorem that enables the velocity potential to be represented as a distribution of sources and/or normal dipoles over boundaries. The chosen linear BEM represents the velocity potentials due to radiation and scattering as a distribution of sources and normal dipoles over the mean submerged body surface. The sources and normal dipoles satisfy the classical linearized free-surface condition and the radiation condition in the frequency domain. Infinite water depth is considered. An integral equation follows by satisfying the linearized body boundary conditions.

The mean submerged surface of the platform is represented by a large number N of small quadrilateral panels. The source strength and dipole moment are assumed constant on each panel and give a total of N unknowns and a total of N linear equations for the unknown source strengths. These equations are solved using methods from linear algebra. Once the potential is obtained, the pressure can be computed, and forces and moments can be obtained to compute body motions.

The commented before is just a brief summary of the theory used in linear frequency-domain BEMs to compute wave loads on floating bodies. A very good reference for this theory is Ref. [18]. More information can also be obtained in Refs. [19–22].

3.2 Time-Domain Boundary Element Method.
The second code used, AEGIR, is a boundary element method that solves the potential flow past a moving or fixed floating body in time domain. It considers non-linear effects such as wet surface variation and it performs Taylor expansions of the boundary conditions.

The time domain boundary element method uses spline functions to represent unknowns and solves the set of equations on the exact body and free surface boundary for the spline coefficients. The geometry is represented by a set of surfaces on the outer boundary of the platform. Moreover, the code is geometrically independent because both the hydrodynamic and the geometry representations are separate. The implication of this statement is that the geometry can be defined in different formats with the only requirement that the surfaces defined must be twice-differentiable with respect to the parametric coordinates.

Within the time-domain boundary element method, the platform is free to sink, trim, and surge. Hydrostatic and hydrodynamic forces and moments are computed from the platform's geometry and the boundary integral equation. During the non-linear calculations, the intersection between the free surface and the platform is calculated. Given the wet part of the platform's surface, a transformation is made to define the computational space.

Normally, a low-order Rankine BEM obtains a system of linear equations by discretizing the obtained equation after applying Green's second identity to the Laplace equation. In the time domain boundary element method, the perturbation potential is approximated as a B-Spline surface in the wet hull parametric space. Moreover, an adaptive subdivision method is used to integrate in the wet surface space.

In relation to the total time-domain potential, Ψ, it is decomposed into the sum of the mean base flow potential, Φ, and the time-dependent wave potential, ϕ. The mean base flow potential is set to zero since our problem does not involve current and forward speed.

The dynamic and kinematic free surface conditions are imposed separately. This is done to seek numerical stability. This way the kinematic condition is solved explicitly and the dynamic condition is solved implicitly.

The kinematic and dynamic free surface conditions are both expanded in a Taylor-series about the base flow.

More details of the theory behind time domain nonlinear boundary element methods can be found in Refs. [10–13].

3.3 Time-Domain Viscous Model. In this section, a description of the viscous volume of fluid URANS code STAR-CCM+ is provided. Turbulent flow is implicitly assumed, and a smooth body surface is considered. The equations solved are the averaged continuity and momentum equations for incompressible fluids where there are no body forces in the floating object.

$$\frac{\partial(\rho\overline{u}_i)}{\partial x_i} = 0 \tag{7}$$

$$\frac{\partial(\rho\overline{u}_i)}{\partial t} + \frac{\partial}{\partial x_j}(\rho\overline{u}_i\overline{u}_j + \rho\overline{u'_iu'_j}) = \frac{\partial\overline{p}}{\partial x_i} + \frac{\partial\overline{\tau}_{ij}}{\partial x_j} \tag{8}$$

$$\overline{\tau}_{ij} = \mu\left(\frac{\partial\overline{u}_i}{\partial x_j} + \frac{\partial\overline{u}_j}{\partial x_i}\right) \tag{9}$$

where $\overline{\tau}_{ij}$ in Eq. (8) are the components of the averaged viscous force tensor, $\overline{p}$ is the averaged pressure, and $\overline{u}$ are the Cartesian components of the averaged velocity. In Eq. (8), $\overline{u'_iu'_j}$ are the Reynolds stresses, ρ is the fluid density, and μ is the dynamic viscosity. To obtain the desired mesh resolution in the boundary layer, $y+$-values near the platform surface must remain below a certain threshold. In Ref. [2], $y+$-values of around 50 provide a good approximation. The definition of $y+$ is $y+ = y \cdot v^*/\nu$, where y is a coordinate perpendicular to the body surface with $y = 0$ at the body surface. v^* is the friction velocity and is expressed as the square root of the ratio between the absolute value of the wall shear stress and the fluid density. Furthermore, $\nu = \mu/\rho$. The viscous sublayer is assumed to be below the given $y+$ values. Given $y+$ values in the simulations of 55 on average (Table 2), the discretization of the integral formulation of the Navier–Stokes equations requires a turbulence model. The two turbulence models mainly used are k-ϵ and k-ω. The model that has been used in these simulations is a combination of the two, the SST k-ω Menter turbulence model [23]. This turbulence model mixes the two previous models using the k-ϵ in areas away from the walls and the k-ω when calculating near to the walls, where boundary layer develops.

To model the free surface, the time-domain viscous model uses a volume of fluid (VOF) method [24]. This model assumes that the same equations governing the physics of one of the phases can be solved for all phases present in the computational domain (each cell or finite volume). A good reference for the theory behind this type of numerical method can also be found in Ref. [25].

In order to simulate the behavior and to obtain realistic platform motions, a dynamic fluid body interaction (DFBI) model is used. The platform is allowed to move in three degrees-of-freedom, to translate in the longitudinal and vertical directions (surge & heave) and to rotate around the transversal direction (pitch).

It is necessary to identify constraints to define the time-step. These constraints depend on the physics that have to be simulated. The objective is to record the following physical phenomena:

(1) Heave, pitch, and surge platform motions.
(2) The waves that travel on the free surface throughout time.

For the heave, pitch, and surge movements, the ITTC recommends at least 100 time-steps per period of encounter with the waves [1,26,27]. The period of encounter, and wave period, ranges from 10–30 s, so 0.1–0.3 s is the minimum time-step regarding the motions. Furthermore, the Courant number (CNN) on the free surface should stay below 0.1. A time-step convergence is performed analyzing both the CNN and the wave elevation at one point using a wave probe. The resultant time-steps of the 11 cases simulated are presented in Table 1. The wave probe is also used to perform the mesh convergence (Fig. 2) giving data to compare with the theoretical wave output. An example of the wave prove for the final mesh selected is presented in Fig. 3.

The platform, as it can be seen in Fig. 4, is positioned $1 \cdot \lambda_w$ from the velocity inlet. The platform is positioned with a maximum

Table 1 The columns indicate wave period (T_w), wave length (λ_w), wave amplitude (ξ_a), and fixed time step (T_s) used in the URANS solver, respectively

T_w (s)	λ_w (m)	ξ_a (m)	T_s (s)
10.00	156.131	2×0.3860	0.012
13.00	263.861	2×0.6515	0.0155
15.00	351.293	2×0.8675	0.0179
16.00	399.702	2×0.9855	0.0190
16.73	437.523	2×1.0800	0.0199
18.00	505.864	1.2490	0.023
19.00	563.633	1.3915	0.023
19.50	593.688	1.4660	0.023
20.00	624.524	1.5420	0.024
21.00	688.538	1.7000	0.025
30.00	1405.179	3.4695	0.036

Note: The waves are within the linear assumption. A minimum wave amplitude was needed to keep the quality of meshes and accelerate convergence.
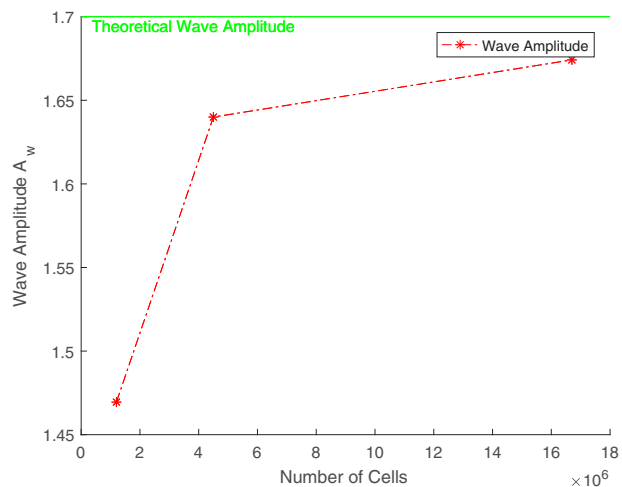

Fig. 2 Wave probe in the undisturbed region, longitudinally located at the platform's center of gravity (without the platform present), and transversally located at $\frac{4}{5}$ of the width of the computational domain. For the wave mesh convergence, three levels of mesh resolution were used. The wave amplitude obtained through a fast Fourier transform is plotted in the figure above and compared to the theoretical wave amplitude. The mesh used in the study is the second which has a 3.5% difference with the theoretical wave amplitude.

distance to the symmetry plane of $B_{max}/2$ to be able to impose a symmetry condition (Fig. 5).

An hexahedral volume mesh is used for the *Background* and *Overset* regions that are overlapped (Chimera grid). Additionally, prism layers are introduced in the *Overset Region*, around the platform surface boundary.

The sizes of the domains *Block Region* and *Overset Region* are chosen using best practices derived from previous seakeeping studies with STAR-CCM+. Good examples are Refs. [1] and [28]. The dimensions of the platform and waves are used to perform the necessary proportions. The water depth is 1/2 of the largest wavelength, which should give negligible finite water depth errors. The final measures for this particular case, here $L_p = 63.5$ is the length of the platform, are the following:

(1) Length: $5.6 \cdot \lambda_w$.
(2) Width: $50 \cdot L_p$.
(3) Depth: $11 \cdot L_p$.

A series of volume controls have been applied to generate an unstructured grid with the necessary refinements to capture the
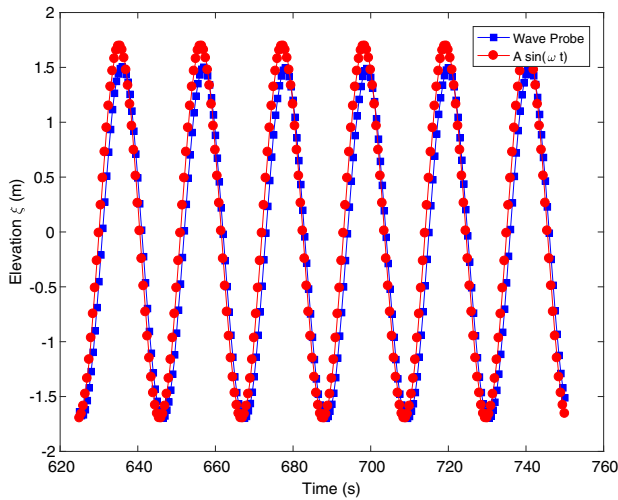
Fig. 3 Wave probe in the undisturbed region, longitudinally located at the platform's center of gravity (without the platform present) and transversally located at $\frac{4}{5}$ of the width of the computational domain. The wave period is 30 s and wave amplitude 1.7 m. The signal obtained is compared to the theoretical profile of a first-order Stokes wave. Discrepancies are due to the surface capturing technique and mesh resolution across the free surface. To account for this, we consider the wave amplitude obtained by applying a Fast Fourier technique (see Fig. 9(b)) to the numerical wave profile (blue line). (Color version online.)

different physical scales that characterize the problem studied. These volume controls are described in the Fig. 6. The mesh refinements in the volume controls have been defined in relation to the wave dimensions and the estimated boundary layer size. These dimensions are presented in Table 2. The volume refinements used are as follows:

(1) *Water Ref 1*: the main purpose of this refinement is to establish continuity in the vertical dimension of the mesh while providing an expansion of the mesh in the horizontal plane. The expansion is done with the objective of creating numerical dissipation at the end of the domain before the *Pressure Outlet*. The objective is to damp out the waves that enter the domain to eliminate any possible reflections in the *Pressure Outlet* that introduce perturbations in the solution.

(2) *Water Ref 2*: this volume control intends to provide an adequate continuum for the wave to propagate uniformly, with minimal numerical dissipation. Regarding the length of *Water Ref 2* refinement ($3.5 \cdot \lambda_w$), it is advised that this length is at least equal to twice the length of the wave simulated (Fig. 6).

(3) *Platform refinement*: the purpose of this volume control is to provide higher grid resolution in the area near the platform.
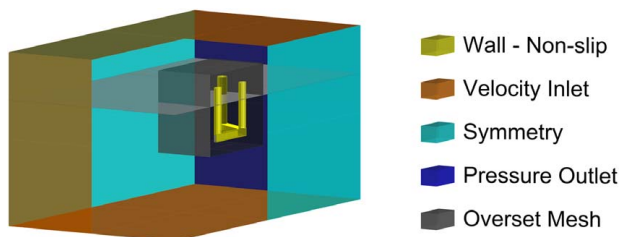

Fig. 4 Representation of the boundary conditions using a color code. Relative dimensions between the floating body and the computational domain have been modified to allow for better visualization (here and in Fig. 5). (Color version online.)
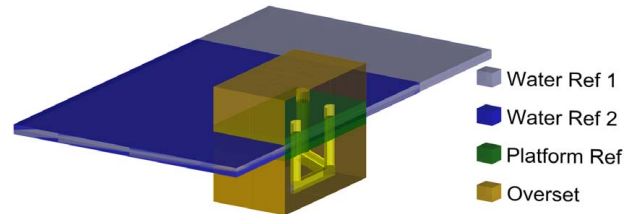

Fig. 5 Representation of the mesh volume controls using a color code

The surface control used is the following:

(1) *Hull*: the surface size control has been created to represent the platform's geometry accurately. Moreover, this enables a good quality prism layer expansion.

The mesh and time convergence has been divided into three steps:

(1) *Convergence of the Block Region mesh*, for the monochromatic wave. This has proven the most important in the convergence of the results. Best practices from previous validations have been taken to define the mesh refinements, such as those found in Ref. [28]. According to this publication, good results can be obtained with approximately 20 cells per wave height and 100 cells per wavelength. The results from the performed mesh convergence are presented in Fig. 2 and Table 3. The final mesh dimensions, relative to the wave dimensions in the simulations, are exposed in Table 2. The sharpening factor is left at 0.0, so there is no term for numerical diffusion in the volume fraction transport equation.

(2) *Convergence of the remaining volume refinements*. Additional volume refinements are created to provide the right domain dimensions and appropriate refinement for the *Overset Region*, and a long enough numerical beach at the end of the domain.

(3) *Convergence of the platform's surface size and boundary layer mesh (prism layer)*. As in the first point, recommendations from Ref. [28] have again been followed. Ten prism layers have been used, with a growth rate factor of 1.3 and $y+$ values are 55 on average (Tables 2 and 3). Consequently, wall functions are necessary to perform the simulations.

Boundary conditions have been defined according to the particularities of the problem. Note that multiple boundary conditions can
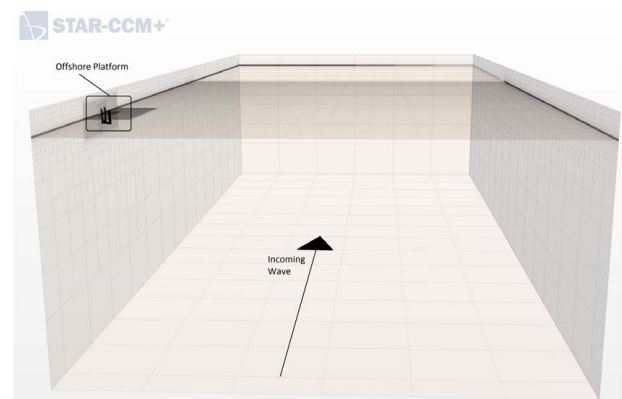

Fig. 6 Example of the computational domain of the shortest wave ($T_w = 18$ s, $A_w = 1.249$ m). The mesh expands transversally, in the y-direction, starting approximately at the lateral mid-length and in the x-direction creating a numerical beach $2 \cdot \lambda_w$ long. Further mesh refinements are done near the platform, the results of these refinements can be seen in Fig. 7. (Color version online.)

Table 2 Mesh characteristics for each of the 11 URANS simulations

	# of cells total	# of cells Overset	$y+$	Overset			Platform Ref. 1			Water Ref. 1			Water Ref. 2		
				X	Y	Z	X	Y	Z	X	Y	Z	X	Y	Z
M1($T_w = 10.00$ s)	6,406,710	861,154	45	$\frac{\lambda_w}{255}$	$\frac{\lambda_w}{255}$	$\frac{H_w}{17}$	$\frac{\lambda_w}{85}$	$\frac{\lambda_w}{85}$	$\frac{H_w}{17}$	Expand	Expand	$\frac{H_w}{17}$	$\frac{\lambda_w}{85}$	$\frac{\lambda_w}{85}$	$\frac{H_w}{17}$
M2($T_w = 13.00$ s)	8,064,141	1,051,344	46	$\frac{\lambda_w}{255}$	$\frac{\lambda_w}{255}$	$\frac{H_w}{17}$	$\frac{\lambda_w}{85}$	$\frac{\lambda_w}{85}$	$\frac{H_w}{17}$	Expand	Expand	$\frac{H_w}{17}$	$\frac{\lambda_w}{85}$	$\frac{\lambda_w}{85}$	$\frac{H_w}{17}$
M3($T_w = 15.00$ s)	4,918,997	654,759	51	$\frac{\lambda_w}{255}$	$\frac{\lambda_w}{255}$	$\frac{H_w}{17}$	$\frac{\lambda_w}{85}$	$\frac{\lambda_w}{85}$	$\frac{H_w}{17}$	Expand	Expand	$\frac{H_w}{17}$	$\frac{\lambda_w}{85}$	$\frac{\lambda_w}{85}$	$\frac{H_w}{17}$
M4($T_w = 16.00$ s)	4,022,589	1,536,357	73	$\frac{\lambda_w}{255}$	$\frac{\lambda_w}{255}$	$\frac{H_w}{17}$	$\frac{\lambda_w}{85}$	$\frac{\lambda_w}{85}$	$\frac{H_w}{17}$	Expand	Expand	$\frac{H_w}{17}$	$\frac{\lambda_w}{85}$	$\frac{\lambda_w}{85}$	$\frac{H_w}{17}$
M5($T_w = 16.73$ s)	3,269,859	1,952,057	55	$\frac{\lambda_w}{255}$	$\frac{\lambda_w}{255}$	$\frac{H_w}{17}$	$\frac{\lambda_w}{85}$	$\frac{\lambda_w}{85}$	$\frac{H_w}{17}$	Expand	Expand	$\frac{H_w}{17}$	$\frac{\lambda_w}{85}$	$\frac{\lambda_w}{85}$	$\frac{H_w}{17}$
M6($T_w = 18.00$ s)	4,147,718	2,703,786	49	$\frac{\lambda_w}{85}$	$\frac{\lambda_w}{255}$	$\frac{H_w}{17}$	$\frac{\lambda_w}{85}$	$\frac{\lambda_w}{85}$	$\frac{H_w}{17}$	Expand	Expand	$\frac{H_w}{17}$	$\frac{\lambda_w}{85}$	$\frac{\lambda_w}{85}$	$\frac{H_w}{17}$
M7($T_w = 19.00$ s)	7,728,123	2,703,715	50	$\frac{\lambda_w}{255}$	$\frac{\lambda_w}{255}$	$\frac{H_w}{17}$	$\frac{\lambda_w}{85}$	$\frac{\lambda_w}{85}$	$\frac{H_w}{17}$	Expand	Expand	$\frac{H_w}{17}$	$\frac{\lambda_w}{85}$	$\frac{\lambda_w}{85}$	$\frac{H_w}{17}$
M8($T_w = 19.50$ s)	4,272,912	1,803,118	48	$\frac{\lambda_w}{255}$	$\frac{\lambda_w}{255}$	$\frac{H_w}{17}$	$\frac{\lambda_w}{85}$	$\frac{\lambda_w}{85}$	$\frac{H_w}{17}$	Expand	Expand	$\frac{H_w}{17}$	$\frac{\lambda_w}{85}$	$\frac{\lambda_w}{85}$	$\frac{H_w}{17}$
M9($T_w = 20.00$ s)	4,624,096	1,803,118	46	$\frac{\lambda_w}{255}$	$\frac{\lambda_w}{255}$	$\frac{H_w}{17}$	$\frac{\lambda_w}{85}$	$\frac{\lambda_w}{85}$	$\frac{H_w}{17}$	Expand	Expand	$\frac{H_w}{17}$	$\frac{\lambda_w}{85}$	$\frac{\lambda_w}{85}$	$\frac{H_w}{17}$
M10($T_w = 21.00$ s)	4,844,652	1,803,120	40	$\frac{\lambda_w}{255}$	$\frac{\lambda_w}{255}$	$\frac{H_w}{17}$	$\frac{\lambda_w}{85}$	$\frac{\lambda_w}{85}$	$\frac{H_w}{17}$	Expand	Expand	$\frac{H_w}{17}$	$\frac{\lambda_w}{85}$	$\frac{\lambda_w}{85}$	$\frac{H_w}{17}$
M11($T_w = 30.00$ s)	4,022,589	1,727,886	55	$\frac{\lambda_w}{255}$	$\frac{\lambda_w}{255}$	$\frac{H_w}{17}$	$\frac{\lambda_w}{85}$	$\frac{\lambda_w}{85}$	$\frac{H_w}{17}$	Expand	Expand	$\frac{H_w}{17}$	$\frac{\lambda_w}{85}$	$\frac{\lambda_w}{85}$	$\frac{H_w}{17}$

Note: The mesh sizes range between 4 and 8 million cells and average $y+$ values remain below 55, limiting the viscous sublayer along the body surface. The mesh refinements are defined in relation to the wavelength (λ_w) and wave height (H_w). The number of cells per wave height and wavelength remains constant through the different cases. Within some control volumes, the mesh is allowed to expand until otherwise specified, so as to create a numerical beach. There are a minimum of eight equal sized cell layers per transition.

Table 3 Results of the convergence of the RAOs in a mesh sensitivity analysis considering four levels of refinement

	Mesh sensitivity analysis											
	18 s				19 s				19.5 s			
T_w Mesh	$e_{RAO_{33}}$	$e_{RAO_{55}}$	# cells	$y+$	$e_{RAO_{33}}$	$e_{RAO_{55}}$	# cells	$y+$	$e_{RAO_{33}}$	$e_{RAO_{55}}$	# cells	$y+$
MR1	29%	5%	1,986,156	424	9%	11%	1,535,684	377	9%	6%	858,326	356
MR2	30%	4%	2,982,100	317	7%	9%	2,531,821	315	11%	6%	2,030,050	305
MR3	8%	1%	5,791,269	167	4%	1%	6,350,109	157	2%	2%	3,098,014	137
Final	0%	0%	7,169,364	49	0%	0%	7,728,123	50	0%	0%	4,272,912	48
	20 s				21 s				30 s			
T_w Mesh	$e_{RAO_{33}}$	$e_{RAO_{55}}$	# cells	$y+$	$e_{RAO_{33}}$	$e_{RAO_{55}}$	# cells	$y+$	$e_{RAO_{33}}$	$e_{RAO_{55}}$	# cells	$y+$
MR1	3%	10%	868,428	361	0%	15%	958,777	351	0%	5%	806,101	331
MR2	3%	10%	2,040,152	303	1%	11%	2,130,535	280	1%	2%	1,978,225	160
MR3	2%	3%	3,449,200	131	1%	4%	3,669,770	119	0%	0%	2,727,964	105
Final	0%	0%	4,624,096	46	0%	0%	4,844,652	40	0%	0%	4,022,589	55

Note: Convergence is quickly reached in all wave periods except for $T_w = 18$ s. For this reason mesh Final is used. $e_{RAO_{33}}$ and $e_{RAO_{55}}$ define errors relative to the finest mesh simulated for each wave period (T_w).

be right for this same problem. Exploiting the symmetry of the problem, given by the incoming head wave condition, only half of the symmetric platform is modeled. The boundary conditions used are illustrated in Fig. 4, using a color code.

A numerical beach has been created in the area before the *Pressure Outlet* that is within the range of $2 \cdot \lambda_w$ times the wavelength used, to avoid numerical wave reflections from the outlet. This boundary condition reduces the vertical velocity of fluid particles by applying damping to the movement in that direction. The guidelines stated in Ref. [29] have been followed to setup the induced damping.

Two reference frames are used for the computations. First, the problem of flow and magnitude of the resultant force over the body is calculated. Then, forces and moments are translated to the local reference system of the platform. This reference system has its origin in the platform's center of gravity, with the *x*-axis in the fore-aft direction. Given these resultant forces, the movement of the platform is calculated. There is no force restraining the model to drift (Figs. 7 and 8).

4 Results

In this section, we briefly illustrate the post-processing process and give a critical overview of the results for each set of simulations. The end result for each set is the heave and pitch RAOs of the platform. By RAO, we mean the amplitude of heave and pitch at the incident frequency divided by the incident amplitude in steady-state oscillatory conditions. Since the calculations by the URANS solve non-linear effects, the RAOs will depend on the incident wave amplitude.

Once RAOs are calculated with frequency and time-domain BEMs, they are examined for areas with large motions and cancellation effects, where viscous phenomena are likely to be significant. As commented before, viscous forces are probable to be important when the platform is oscillating near its natural period.

Importance of cancellation effects is given by *red*, the probability of occurrence of the wave periods at which it materializes ($T_w = 15$–17 s) and the unconventional geometry analyzed, which may not have a cancellation period as it has been shown in experiments
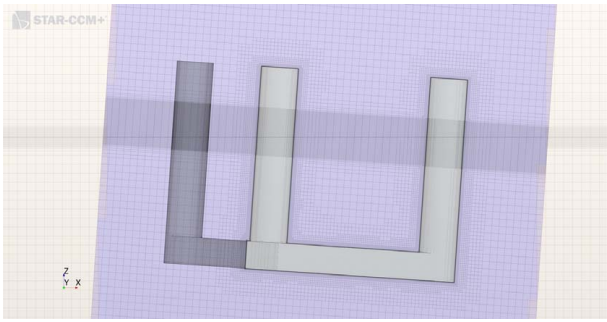
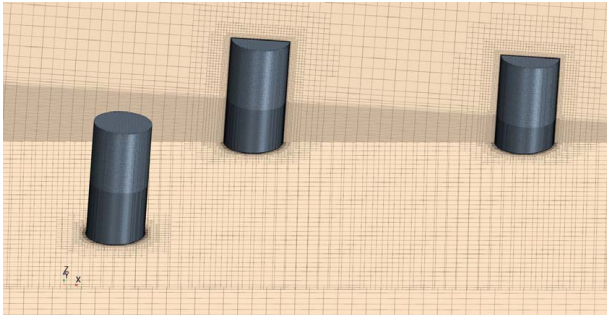**Fig. 7 Second example of a mesh near the platform at a time instant during the simulation**

Fig. 8 Example of a mesh near the platform at a time instant during the simulation. The overset domain is $1.5 \cdot L_p$ long, $1.5 \cdot B_p$ wide, and $1.8 \cdot D_p$ deep. The platform is centered within the overset domain.

for other unconventional geometries [30]. They correspond to severe weather conditions that can have return periods clearly inferior to 50 years in many potential locations for offshore wind energy. BEM methods with no viscous dissipations give a particular misleading picture of this situation. They predict negligible heave motions. Additional difficulties have been encountered when correcting the potential codes near the cancellation period. Unphysical amounts of empirical damping would be needed to obtain a good approximation in the proximity of the cancellation period. Therefore, the class of functions approximated by potential numerical methods are not rich enough to fully characterize RAOs of the studied semi-submersible platform geometry.

In these situations, nonlinear phenomena such as vortex shedding will affect the motions by modifying pressure loads on the platform (Fig. 12(b)). For this reason, this type of situations are simulated in the high-fidelity viscous code. The motions of the platform are calculated for 11 different monochromatic waves (Table 1) that discretize the region around the natural heave, pitch, and heave cancellation periods of the platform, obtained from the frequency-domain BEM, time-domain BEM, and analytical relations (Table 4 and Eq. (6)). The first and last waves are simulated to ensure that the same RAO is obtained for cases where the viscous and non-linear phenomena are not significant and all codes used should output the same result. Table 4 contains a brief summary of the main dimensions and mass properties of the platform.

The data obtained from the time domain programs needs to be post-processed in order to be able to compare to the results of the frequency-domain BEM. These intermediate results are as follows:

(1) *Heave time history*: longitudinal displacement along the vertical direction of the platform.
(2) *Pitch time history*: rotation around the transversal direction of the platform.

Table 4 Principal dimensions and mass properties of the platform

Length (L_p)	63.5 m
Beam (B_p)	36.0 m
Depth (D_p)	44.0 m
Radius of the columns (R_c)	4.0 m
Height of the pontoons (H_p)	6.0 m
Width of the pontoons (B_p)	8.0 m
Length of the pontoons (L_p)	37.0 m
Draft (T_p)	30.0 m
Displacement (Δ)	$1.071 \cdot 10^7$ kg
Radius of gyration (r_{xx})	26.4 m
Radius of gyration (r_{yy})	26.4 m
Radius of gyration (r_{zz})	20.5 m
Vertical center of gravity z-coordinate	−20.3 m
Heave natural period	19.45 s
Pitch natural period	19.00 s

Note: The natural periods are estimated by: $T_{ii} = 2\pi \cdot \sqrt{(M_{ii} + A_{ii})/C_{ii}}$.

(3) *Surface elevation time history (incident wave)*: distance of the free surface to the $z = 0$ plane at a point located in the undisturbed region, longitudinally located at the platform's center of gravity and transversally located at $\frac{4}{5}$ of the width of the computational domain.

To calculate the RAO from the time series of the movement and wave elevation a Fast Fourier Transform is done. Then, it is just a matter of obtaining the RAO from the following well-known formula in spectral analysis:

$$\phi_{xi}(\omega) = RAO^2 \cdot \phi_{\xi}(\omega) \qquad (10)$$

To ensure that the time series is long enough, the convergence of the RAO is analyzed throughout the length of the time history recorded (Fig. 9(d)). In Fig. 9, an example of the intermediate and final outputs of the time histories' analysis process is provided.

When the post-processing is completed, the results can be compared in a plot, such as in Fig. 10. In this figure, it can be seen that there is a very good agreement between the frequency-domain BEM and the time-domain BEM. On the other hand, although the short ($T_w = 18$ s) and the long ($T_w = 30$ s) wave of the URANS simulation set perfectly match (results are within 2%) the predicted RAO by the potential codes, the latter largely overpredicts the motions, which take the form of a spike, as you approach the natural period. The reason for this is that potential codes can only consider potential flow radiation damping which tends to diminish with the wavelength and, in the particular case of the geometry simulated, tends to be very small near the heave and pitch natural periods (Table 4). In Fig. 11, the heave and pitch potential damping is represented as a function of the wave period, showing how small the potential radiation damping is near the heave and pitch natural periods. Consequently, when we simulate the platform in wave periods near this minimum, adding on top the strong coupling between the two motions, the response is greatly augmented. A possibility to mitigate this is to add a certain quantity of viscous damping.

An example of the captured vortex shedding in the URANS simulations is presented in Fig. 12(b). In this figure, the field *vorticity magnitude* can be visualized in an *xz*-plane parallel to one of the horizontal legs. The consequence of vortex shedding is important viscous pressure loads.

In the calculation of RAOs, monocromatic waves are used in the time domain numerical methods. In practice, wave spectra should be used to capture second difference frequency effects [33–35], which can have important effects on the resonance responses in heave and pitch. The choice of using monochromatic waves was made to have an easier direct comparison of all three numerical methods, when all predicted responses can be considered as linear. This is done at the expense of narrowing the range of non-linear phenomena that time domain solvers could capture.
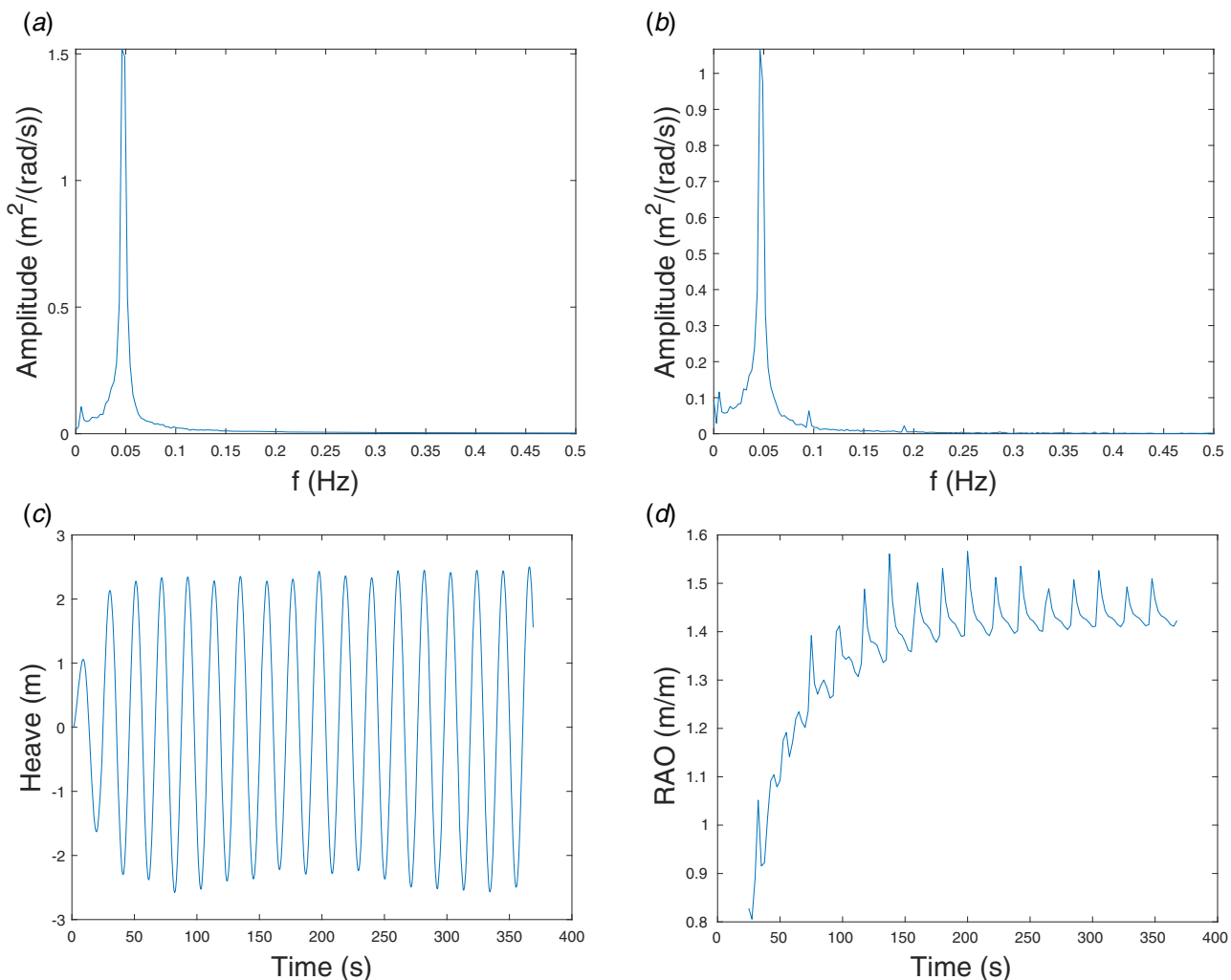
Fig. 9 Example of the output of the analysis process of the motion time histories. The time traces correspond to the URANS motion analysis of the $T_w = 20$ s wave. The data plotted in Figs. 9(a) and 9(b) are used to obtain the RAO through Eq. (10). This is done as the time simulated increases to check for convergence (Fig. 9(d)). The wave elevation spectra is taken to consider any mesh effects and small errors in the numeric calculations, as explained in Fig. 3. (a) Spectrum of heave motion $H(t)$ in amplitudes, (b) spectrum of surface elevation $\xi(t)$ in amplitudes, (c) heave time history, and (d) RAO convergence with the increase of time simulated.

In the last step of the analysis, a viscous correction has been introduced in the frequency and time-domain BEMs. Empirical corrections can range 3–10% of the critical damping. In this study, the best fit, for both frequency and time-domain BEMs, is given by 6.25% and 6.6% of the critical damping, in heave and pitch, respectively. With this correction, it can be said that potential codes provide a very good motion prediction only requiring URANS near the resonance period.

4.1 Non-Linear Decoupled Heave Equation With Empirical Coefficients. In order to assess viscous drag forces, we will use experimental [36] and numerical [37] drag coefficients for a facing square at small Keulegan–Carpenter numbers. Since the considered Reynolds numbers are relatively small in their studies, viscous shear forces due to laminar flow are not negligible even though they are small relative to pressure loads. However, using empirical formula for shear stress by Ref. [38] with ambient harmonically oscillating flow along a fixed plane surface with turbulent boundary layer flow show that the shear stress can be neglected in full scale relative to pressure drag. This means that an estimate of the drag coefficient for a facing square at small Keulegan Carpenter numbers and full-scale conditions will be based on neglecting the

effect of the shear stress in the boundary layer flow. Furthermore, we assume that the pressure drag are the same in model and full scale due to the fact that the separation points are the same in model and full scale. Berthelsen and Faltinsen [37] predict that the grid-independent drag coefficient is 3.42 for a facing square at $\beta = 213$ and Keulegan-Carpenter number KC = 1.5. Here, $\beta = B^2/(\nu T)$ is the ratio between Reynolds number and KC-number with B and T as the width of the section and oscillation period of the ambient flow, respectively. We deduct the in-line drag coefficient associated with the frictional force in phase with the ambient velocity and get $C_D = 2.92$. The fact that the width to height ratio 8/6 for the pontoons is higher than for a square section is likely to cause a higher drag coefficient [39,40]. They used a single vortex method which suggests a C_D value of 3.10 for the rectangular cross section of the pontoons at KC = 1.5. However, the KC dependence of C_D is low at small KC numbers. The fact that the drag coefficient is KC-dependent will be indirectly accounted for by considering how reasonable uncertainties in the estimated drag coefficient affect the heave amplitude. It is difficult in a simple way to account for the intersections between the pillars and the pontoons. One consideration is the number of corners where the flow separates at a cross section of a pontoon. If we consider the pillars at the ends of the pontoons, then there are four corners until
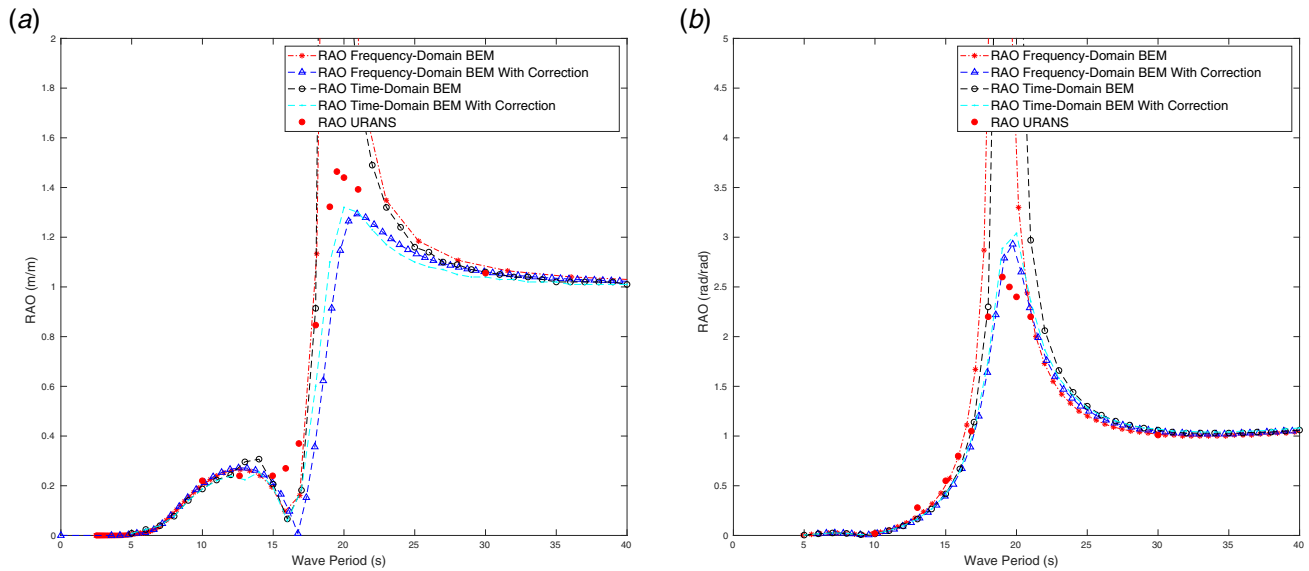
(a)

(b)

Fig. 10 Comparison of the RAOs obtained from the frequency-domain BEM, time-domain BEM, corrected frequency-domain BEM, corrected time-domain BEM and URANS code. The RAOs presented are referred to the COG, and a complete transformation matrix composed of Euler angles is implemented in the time-domain BEM and URANS simulations. Results from the potential codes above 2 and 4 are discarded, because they are the result of a minimum in the potential radiation damping detailed in Fig. 11. At first, viscous corrections have not been included in the time-domain or frequency-domain potential flow based predictions; afterward, additional damping is introduced. It is commonly accepted that heave and pitch viscous damping of semi-submersible platforms ranges from 3–10% of critical damping, staying around 5% for pitch [31,32]. In this study, the best fit, for both frequency and time-domain BEMs, is given by 6.25% and 6.6% of the critical damping, in heave and pitch, respectively. So, with this conservative correction, both potential codes provide a very good prediction for all cases, only requiring URANS near the resonance and the cancellation period. (a) Heave motion RAOs and (b) pitch motion RAOs.

we are one pillar radius from the end. Two separation corners imply as a first approximation that the drag coefficient is half of the drag coefficient with four separation points. Furthermore, we must notice the effect of different width-to-height ratios of the cross sections at one pillar radius from the end of the pontoons. This has a small effect according to Ref. [39]. Then comes 3D effects which is pronounced at the ends. However, since the KC number is small and the shed vorticity hence stays close to the pontoons, the 3D effect is expected to be smaller than it for instance is for cross-flow past a ship in current as discussed in Ref. [17].

Fig. 11 B_{33} and B_{55} radiation damping coefficients obtained from the frequency-domain BEM. A minimum near the natural period of oscillation generates unrealistically high motions (Fig. 10).

We follow a rough approach to account for 3D end effects of pontoons and introduce the projected area $A_p = 935.1 \text{ m}^2$ of the pontoons as seen from below. At the intersection between the central pillar and the pontoons, we use the same drag coefficient as estimated for the rectangular cross sections. At the other intersections associated with a projected area $A_{pl} = 75.40 \text{ m}^2$, we reduce the drag coefficients by using an average value that is half of the value for the rectangular cross sections. That means the drag coefficient for the platform associated with vertical motions is estimated as

$$C_D = \frac{0.5 \cdot 3.1 \cdot A_{pl} + 3.1\left(A_p - A_{pl}\right)}{A_p} = 2.99 \qquad (11)$$

Viscous effects matter at resonance and the potential-flow cancellation period. In order to model both effects, we will express the viscous loads in the terms of the relative velocity between heave and the vertical incident wave velocity at the pontoon level. The equation of heave motion is therefore expressed as

$$(M + A_{33})\frac{d^2\eta_3}{dt^2} + \underbrace{0.5\rho C_D A_p\left(\frac{d\eta_3}{dt} - w\right)\left|\frac{d\eta_3}{dt} - w\right|}_{B_V}$$
$$+ \underbrace{\rho g A_W}_{C_{33}}\eta_3 = F_3(t) \qquad (12)$$

where

$$F_3(t) = \rho g \xi_a \sin(\omega t) e^{kz_m}\left(A_W e^{k(z_t - z_m)} - k\left(V_p + \frac{A_{33}}{\rho}\right)\right) \qquad (13)$$

$$w = \omega \xi_a e^{kz_m}\cos(\omega t) \qquad (14)$$

Equation (12) is integrated with initial values and the heave amplitude in steady-state oscillatory conditions is found for different wave periods [41–44].
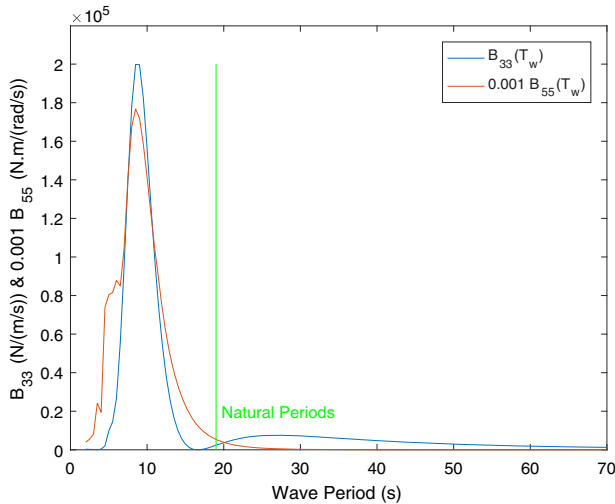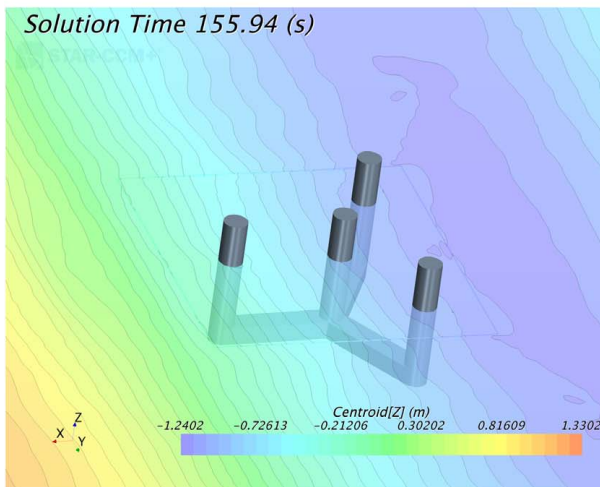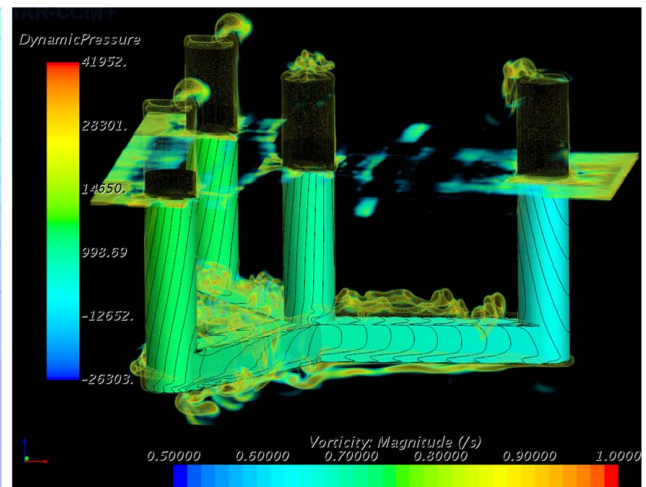
(a)

(b)

Fig. 12 In Fig. 12(a), the wave elevation is plotted and, in Fig. 12(b), non-linear phenomena at platform's natural period ($T_w = 19$ s) can be seen. In Fig. 12(b), the color map represents the module of the vorticity field. As it can be observed in the image, the vorticity is mainly generated by the horizontal legs of the offshore platform. (a) Wave elevation and (b) magnitude of the vorticity field. (Color version online.)

Additionally, the estimated C_D value from experimental results is compared against a C_D value calculated from a decay test. We consider the equation of motion $\ddot{x} + p_1\dot{x} + p_2|\dot{x}|\dot{x} + p_3 x = 0$. The decay tests are performed with the URANS solver. By analyzing Fig. 13, we can fit Eq. (15) with least mean squares.

$$\frac{2}{T_m}\log\left(\frac{X_{n-1}}{X_{n+1}}\right) = p_1 + \frac{16X_n}{T_m}p_2 \qquad (15)$$

where T_m is the mean oscillation period. Between X_n and X_{n+1}, there is one half period $T_m/2$ for any n. The coefficients p_1 and p_2 are the linear and quadratic damping terms, respectively. Using the area of the platform as seen from below, we obtain $C_D = 2.83$ which confirms the previous estimations that predict $C_D \sim 3.00$.

To evaluate the performance of this simplified model, the heave motion predictions are plotted alongside the URANS predictions in Fig. 14. This comparison has allowed to provide a rough measure of flow uncertainty which could prevent us from extrapolating results of available experiments. This is especially useful for analyzing the flow at heave cancellation and resonance periods, due to linear waves. Keulegan–Carpenter number in these conditions is 1 inducing high variability in the C_D of the platform. While studying the difference in motion predictions other non-linear phenomena has been observed, although its overall influence in the platform motion has not been rigorously quantified. The first observed non-linear phenomena are vortexes that develop at the edges of the pontoons. These vortexes and the movement of the platform are seen to perturb the wave velocity and pressure fields, potentially making Eq. (13) inaccurate and requiring an increment of the drag coefficient to account for a pressure correction. Average pressure has been recorded on the top and bottom faces of the pontoons and compared to those predicted by potential theory. The recorded pressure is significantly smaller (probably due to vortex shedding) and similar between the top and bottom faces at the heave cancellation period. This has eliminated the cancellation of forces because of the larger bottom pontoon area. Similarly, the predicted excitation
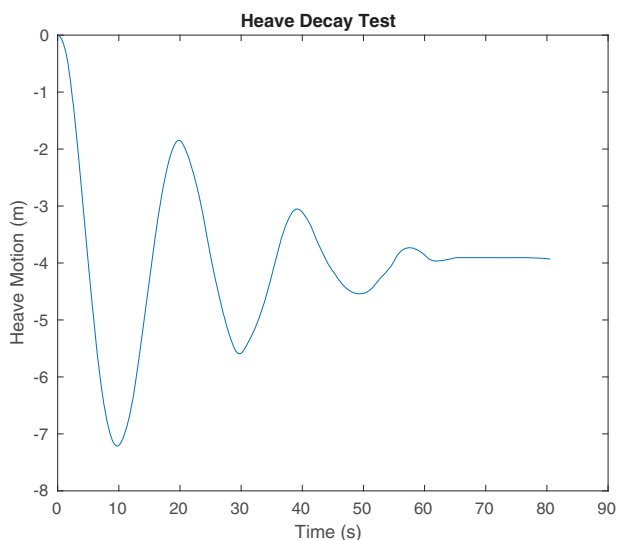

Fig. 13 Evolution of the heave motions during the heave decay test performed in with the URANS solver. Drag coefficient estimated by comparison with experiments ($C_D = 3$).
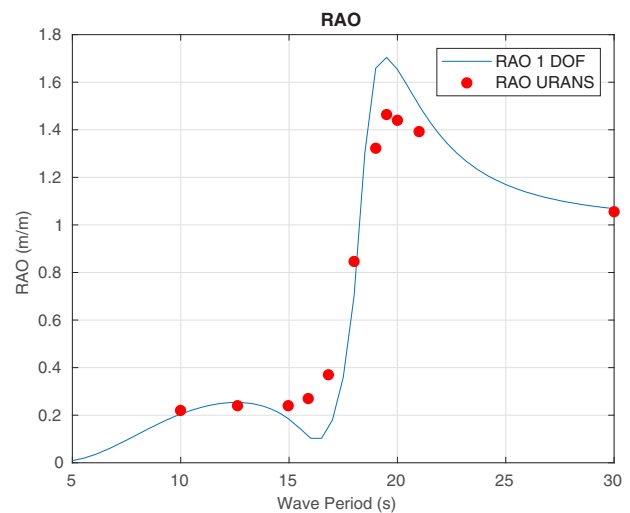

Fig. 14 Comparison between heave RAO predictions performed with the decoupled heave differential equation (Eq. (12)) and the URANS solver. Significant differences can be seen by comparison with URANS. Probably due to non-linear phenomena such as vortex-shedding and perturbation to the velocity and pressure fields due to platform motions.
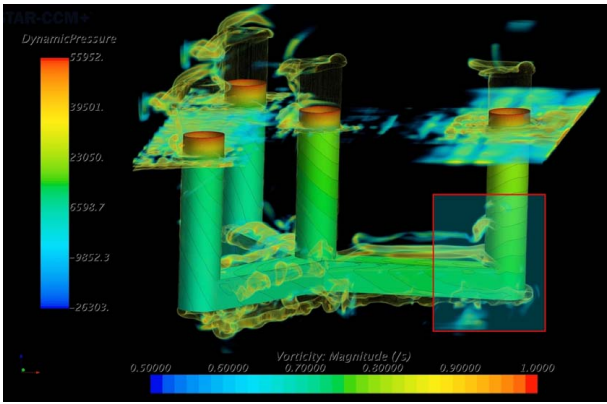
Fig. 15 Vortex sheets being shedded at the platform edges. Flow confinement between the columns introduces perturbation to the vortex sheet development.

forces at the heave resonance period are smaller in the URANS model than in the simplified non-linear potential method.

5 Conclusions

This paper highlights the major characteristics of three different computational techniques and the modeling assumptions at the basis of their formulations. In the performed motion analysis, we prove the feasibility for designers of combining the information from three different numerical models. The paper presents an interesting comparison of the existing numerical methods used for predicting motions of floating objects in waves. Nevertheless, significant emphasis has been placed in the description of the viscous flow solution, obtained using complex multi-phase URANS solver. The paper correctly evidences the limitation of potential flow models in predicting offshore platform motions for waves having periods close to the natural frequency of the system. Corrections coefficients can be included in potential flow predictions, but their entity can just be estimated according, for instance, to previous experimental measurements. Here, we used URANS solver as a virtual replica of the system with the final aim to calibrate the empirical corrections in order to properly predict motions at resonance. We demonstrate that the computational burden of the high-fidelity viscous model with non-linear free surface is justified only when incoming waves induce motions at the resonance frequency, being 175 times more expensive than the time-domain BEM and 700,000 times more expensive than the frequency-domain BEM. For this particular operating condition, both frequency and time domain models largely overestimate the response of the system, leading to large discrepancies if not corrected with empirical terms. However, where there are relatively small motions ($RAO \leq 1$), all codes predict the same motions (Fig. 10) only requiring URANS near the resonance and cancellation periods (Fig. 15).

The large computational burden largely limits the application of URANS simulations in very important design processes such as optimization. High-fidelity URANS predictions have been recently included in the construction of stochastic surrogate models used together with Bayesian optimization techniques. In particular, the use of Gaussian processes have allowed to construct accurate response surfaces by efficiently blending data-sets coming from different fidelity sources (e.g., potential flow and URANS predictions). These response surfaces (surrogate models) are capable of describing quantities of interest such as motions in high-dimensional spaces (for instance operating conditions or designs). Some good examples of this are Ref. [45] where the fidelity of a URANS model was tuned by changing the mesh resolution and Ref. [46] where potential flow and RANSE calm water predictions were

used to optimize the shape of a SWATH vessel. This proves that it is reasonable to think that such optimization techniques can make URANS simulations a practical design and optimization tool.

Nomenclature

g = acceleration of gravity
k = wave number
$\mathbf{n}$ = unit normal vector, Cartesian coordinate system
$\mathbf{x}$ = position vector, Cartesian coordinate system
B = distance between center planes of the two pontoons
M = platform mass
$\bar{u}$ = averaged velocity
$\bar{p}$ = averaged pressure
z_m = coordinate of the geometric center of the pontoons
z_t = coordinate of the top of the pontoons
A_{33} = added mass in heave
A_w = waterplane area
B_{max} = maximum beam
B_p = beam of the platform
D_p = depth of the platform
L_p = length of the platform
S_b = the platform's wet surface
T_p = draft of the platform
T_s = URANS time-step
T_w = wave period
V_p = total volume of the pontoons
$F_3(t)$ = vertical excitation force
$G(\mathbf{x}, \xi)$ = Green function
η_3 = heave motion
λ_w = wavelength
μ = dynamic viscosity
$44\xi_a$ = incident wave amplitude
ξ_j = motion amplitude in direction j
$\bar{\tau}_{ij}$ = components of the averaged viscous force tensor
ρ = fluid density
Φ = mean base flow velocity potential
ϕ = modulus in complex notation of the velocity potential
ϕ_D = diffraction potential
ϕ_I = incident wave potential
ϕ_R = radiation potential
ϕ_{xi} = frequency spectra associated with the ith DOF
ϕ_ξ = frequency spectra associated with free surface elevation
Ψ = total time-domain potential
ω = wave circular frequency
ω_n = natural circular frequency

References

[1] Tezdogan, T., Demirel, Y. K., Kellett, P., Khorasanchi, M., Incecik, A., and Turan, O., 2015, "Full-Scale Unsteady RANS CFD Simulations of Ship Behaviour and Performance in Head Seas Due to Slow Steaming," Ocean Eng., **97**, pp. 186–206.
[2] Ruth, E., Berge, B. O., and Borgen, H., 2015, "Simulation of Added Resistance in High Waves, ASME 2015 34th International Conference on Ocean, Offshore and

Arctic Engineering, St. John's, Newfoundland, Canada, American Society of Mechanical Engineers, p. V011T12A018.

[3] Shen, Z., and Wan, D., 2013, "RANS Computations of Added Resistance and Motions of a Ship in Head Waves," Int. J. Offshore Polar Eng., **23**(4), pp. 264–271.

[4] Bonfiglio, L., Vernengo, G., Brizzolara, S., and Bruzzone, D., 2016, "A Hybrid RANSE–Strip Theory Method for Prediction of Ship Motions," Maritime Technology and Engineering III: Proceedings of the 3rd International Conference on Maritime Technology and Engineering, Lisbon, Portugal, CRC Press, p. 241.

[5] Mousaviraad, M., Conger, M., Stern, F., Peterson, A., and Ahmadian, M., Validation of CFD-MBD FSI for High-Fidelity Simulations of Full-Scale WAM-V Sea-Trials With Suspended Payload.

[6] Mousaviraad, S. M., Bhushan, S., and Stern, F., 2013, "URANS Studies of Wam-v Multi-Body Dynamics in Calm Water and Waves," Third International Conference on Ship Maneuvering in Shallow and Confined Water, Ghent, Belgium, pp. 3–5.

[7] Bonfiglio, L., and Brizzolara, S., 2013, "Influence of Viscosity on Radiation Forces: a Comparison Between Monohull, Catamaran and SWATH," The Twenty-Third International Offshore and Polar Engineering Conference, Anchorage, AL, International Society of Offshore and Polar Engineers.

[8] Bonfiglio, L., and Brizzolara, S. 2018, "Amplitude Induced Nonlinearity in Piston Mode Resonant Flow: A Fully Viscous Numerical Analysis," ASME J. Offshore Mech. Arctic Eng., **140**(1), p. 011101.

[9] Zamora-Rodriguez, R., Gomez-Alonso, P., Amate-Lopez, J., De-Diego-Martin, V., Dinoi, P., Simos, A., and Souto-Iglesias, A., 2014, "Model Scale Analysis of a TLP Floating Offshore Wind Turbine," Proceedings of the ASME 2014 33rd International Conference on Ocean, Offshore and Arctic Engineering, San Francisco, CA.

[10] Kring, D. C., 1994, *Time Domain Ship Motions by a Three-Dimensional Rankine Panel Method*, Massachusetts Institute of Technology.

[11] Kring, D. C., Korsmeyer, F. T., Singer, J., Danmeier, D., and White, J., 1999, "Accelerated Nonlinear Wave Simulations for Large Structures," 7th Int'l Conference on Numerical Ship Hydrodynamics, Nantes, France.

[12] Kring, D. C., Korsmeyer, F. T., Singer, J., and White, J., 2000, "Analyzing Mobile Offshore Bases Using Accelerated Boundary Element Methods," J. Marine Struct., **13**(4–5), pp. 301–313.

[13] Kring, D. C., Milewski, W. M., and Fine, N. E., 2004, "Validation of a NURBS-based BEM for Multihull Ship Seakeeping," 25th Symposium on Naval Hydrodynamics, St. John's, The National Academies Press, Washington, DC.

[14] Beck, R. F., and Scorpio, S. M., 1995, "A Desingularized Boundary Integral Method for Fully Nonlinear Water Wave Problems," Twelfth Australasian Fluid Mechanics Conference, Sydney, Australia, University of Sydney, Sydney, Australia, p. 6.

[15] Cao, Y., Beck, R. F., and Schultz, W. W., 1994, "Nonlinear Computation of Wave Loads and Motions of Floating Bodies in Incident Waves," Proceedings of the 9th International Workshop on Water Waves and Floating Bodies (IWW WFB).

[16] Zhang, X., and Beck, R. F., 2007, "Computations for Large-Amplitude Two-Dimensional Body Motions," J. Eng. Math., **58**(1), pp. 177–189.

[17] Faltinsen, O. M., 1993, *Sea Loads on Ships and Offshore Structures*, Cambridge University Press.

[18] Lee, C-H., and Newman, J. N., 1988, "The Computation of Wave Loads on Large Offshore Structures," Proceedings of the International Conference on Behaviour of Offshore Structures (BOSS'88), Tapir Pubishers, Trondheim, Norway, pp. 605–622.

[19] Newman, J. N., 1977, *Marine Hdrodynamics*, MIT Press.

[20] Newman, J. N., 1985, "Algorithms for the Free-Surface Green Function," J. Eng. Math., **19**(1), pp. 57–67.

[21] Newman, J. N., 1986, "Distributions of Sources and Normal Dipoles Over a Quadrilateral Panel," J. Eng. Math., **20**(2), pp. 113–126.

[22] Lee, C-H., and Newman, J. N., 2005, "Computation of Wave Effects Using the Panel Method," WIT Transactions on State-of-the-Art in Science and Engineering, 18, WIT Press.

[23] Menter, F. R., 1994, "Two-Equation Eddy-Viscosity Turbulence Models for Engineering Applications," AIAA J., **32**(8), pp. 1598–1605.

[24] Hirt, C. W., and Nichols, B. D., 1981, "Volume of Fluid (VOF) Method for the Dynamics of Free Boundaries," J. Comput. Phys., **39**(1), pp. 201–225.

[25] Ferziger, J. H., and Perić, M., 2014, *Computational Methods for Fluid Dynamics*, Springer Science & Business Media.

[26] Perić, M., 2012, "Wave Impact, Body Motion and Overset Grids in STAR-CCM," STAR South East Asian Conference.

[27] Atreyapurapu, K., Tallapragada, B., and Voonna, K., 2014, "Simulation of a Free Surface Flow Over a Container Vessel Using CFD," Int. J. Eng. Trends Technol. (IJETT), pp. 334–339.

[28] Oggiano, L., Pierella, F., Nygaard, T. A., De Vaal, J., and Arens, E., 2016, "Comparison of Experiments and CFD Simulations of a Braceless Concrete Semi-Submersible Platform," Energy Procedia, **94**, pp. 278–289.

[29] Perić, R., and Abdel-Maksoud, M., 2016, "Reliable Damping of Free-Surface Waves in Numerical Simulations," Ship Technol. Res., **63**(1), pp. 1–13.

[30] Robertson, A. N., Wendt, F., Jonkman, J. M., Popko, W., Dagher, H., Gueydon, S., Qvist, J., Vittori, F., Azcona, J., Uzunoglu, E., Soares, C. G., Harries, R., Yde, A., Galinos, C., Hermans, K., de Vaal, J. B., Bozonnet, P., Bouy, L., Bayati, I., Bergua, R., Galvan, J., Mendikoa, I., Sanchez, C. B., Shin, H., Oh, S., Molins, C., and Debruyne, Y., 2017, "C5 Project Phase II: Validation of Global Loads of the DeepCwind Floating Semisubmersible Wind Turbine," Energy Procedia, **137**, pp. 38–57.

[31] Simos, A. N., Ruggeri, F., Watai, R. A., Souto-Iglesias, A., and Lopez-Pavon, C., 2018, "Slow-Drift of a Floating Wind Turbine: An Assessment of Frequency-Domain Methods Based on Model Tests," Renewable Energy, **116**, pp. 133–154.

[32] Pedersen, E. A., 2012, *Motion Analysis of Semi-submersible*, Institutt for Marin Teknikk.

[33] Faltinsen, O. M., 1988, "Second Order Nonlinear Interactions Between Waves and Low Frequency Body Motion," Nonlinear Water Waves. International Union of Theoretical and Applied Mechanics, Springer, Berlin, Heidelberg.

[34] You, J., and Faltinsen, O. M., 2015, "A Numerical Investigation of Second-Order Difference-Frequency Forces and Motions of a Moored Ship in Shallow Water," J. Ocean Eng. Mar. Energy, **1**(2), pp. 157–179.

[35] Faltinsen, O. M., 1990, "Wave Loads on Offshore Structures," Annu. Rev. Fluid Mech., **1**(1), pp. 35–36

[36] Bearman, P. W., Downie, M. J., Graham, J. M. R., and Obasaju, E. D., 1985, "Forces on Cylinders in Viscous Oscillatory Flow at Low Keulegan-Carpenter Numbers," J. Fluid Mech., **154**, pp. 337–356

[37] Berthelsen, P. A., and Faltinsen, O. M., 2008, "A Local Directional Ghost Cell Approach for Incompressible Viscous for Problems With Irregular Boundaries," J. Comput. Phys., **227**(9), pp. 4354–4397.

[38] Johnson, I. G., 1978, "A New Approach to Oscillatory Rough Turbulent Boundary Layers," Series Paper 17, Institute of Hydrodynamic and Hydraulic Engineering. Technical University of Denmark Lyngby.

[39] Faltinsen, O. M., and Sortland, B., 1987, "Slow Drift Eddy Making Damping of a Ship," Appl. Ocean Res., **9**(1), pp. 37–46.

[40] Tanaka, N., Ikeda, Y., and Nishino, K., 1982, "Hydrodynamic Viscous Force Acting on Oscillating Cylinders With Various Shapes," Proceedings of the 6th Symposium of Marine Technology, The Society of Naval Architects of Japan.

[41] ANSYS, AQWA, 2017, Users Manual (ver. 14.0). ANSYS Incorporated, Canonsburg, PA.

[42] AEGIR version 2015, User's Manual.

[43] Ogilvie, T. F., and Tuck, E. O., 1969, "A Rational Theory of Ship Motions, Part 1," Report 013, Dept. of Naval Arch., Univ. of Michigan.

[44] STAR-CCM+ version 12.02. 011, 2017. User's Manual.

[45] Bonfiglio, L., Perdikaris, P., Brizzolara, S., and Karniadakis, G. E., 2017, "Multi-fidelity Optimization of Super-Cavitating Hydrofoils," Computer Methods in Applied Mechanics and Engineering, Elsevier.

[46] Bonfiglio, L., Perdikaris, P., and Brizzolara, S., 2016, "Multi-Fidelity Optimization of High Speed SWATHs," Proceedings of the SNAME Maritime Convention, Bellevue, WA, Nov. 1–5.